Shack–Hartmann centroid detection method based on high dynamic range imaging and normalization techniques

Javier Vargas,[1,*] Luis González-Fernandez,[1] Juan Antonio Quiroga,[2] and Tomás Belenguer[1]

[1]Laboratorio de Instrumentación Espacial, Instituto Nacional de Técnica Aeroespacial, Carretera de Ajalvir Km 4, 28850 Torrejón de Ardoz,Madrid, Spain

[2]Optics Department, Universidad Complutense de Madrid, Facultad de CC. Físicas, Ciudad Universitaria s/n, 28040 Madrid, Spain

*Corresponding author: jvargas@fis.ucm.es

Received 24 November 2009; revised 26 March 2010; accepted 29 March 2010; posted 31 March 2010 (Doc. ID 120455); published 23 April 2010

In the optical quality measuring process of an optical system, including diamond-turning components, the use of a laser light source can produce an undesirable speckle effect in a Shack–Hartmann (SH) CCD sensor. This speckle noise can deteriorate the precision and accuracy of the wavefront sensor measurement. Here we present a SH centroid detection method founded on computer-based techniques and capable of measurement in the presence of strong speckle noise. The method extends the dynamic range imaging capabilities of the SH sensor through the use of a set of different CCD integration times. The resultant extended range spot map is normalized to accurately obtain the spot centroids. The proposed method has been applied to measure the optical quality of the main optical system (MOS) of the mid-infrared instrument telescope smulator. The wavefront at the exit of this optical system is affected by speckle noise when it is illuminated by a laser source and by air turbulence because it has a long back focal length (3017 mm). Using the proposed technique, the MOS wavefront error was measured and satisfactory results were obtained.

OCIS codes: 120.3940, 100.5070, 120.4630, 120.6085.

1. Introduction

Wavefront sensors are used to measure the optical quality of an optical beam. Typical wavefront sensors are Fizeau [1] or shearing interferometers [2] and Shack–Hartmann (SH) devices [3–6]. Advantages of interferometric wavefront sensors are principally their precision and capacity to obtain good results even with low contrast fringes. The main drawbacks are the requirement of a coherent light source and interferometers with an intrinsic phase ambiguity of 2π.

A SH wavefront sensor consists of a two-dimensional microlens array focused on a CCD camera. The measuring principle of a SH sensor is based on the determination of local slopes of an incoming wavefront. An incoming wavefront W is sampled by a microlens array. Each microlens focuses the incident wave into its focal plane where a CCD sensor is placed to capture the spot map. The centroid of each spot is obtained using typical computer vision techniques [7,8] and the resultant centroid map, called the Hartmann spot diagram, is computed. From a high quality reference beam, the displacements $(\Delta x, \Delta y)$ between corresponding centroids of the test and reference beams are calculated. Deviation of corresponding spots yields information about the local slopes of the wavefront error (ΔW), the

0003-6935/10/132409-08$15.00/0

difference between the incoming problem and the reference wavefronts. The wavefront reconstruction process can be distinguished by two general approaches: zonal and modal [9]. Zonal algorithms are based on a straightforward integration of the local slopes [10]. Modal algorithms approximate the wavefront by a linear combination of a number of known aperture related functions, typically Zernike polynomials [9,11,12].

SH sensors are one of the most widely used sensors in optical quality diagnostic processes of imaging optical systems but also in adaptive optics to reduce the atmospheric induced aberrations by their real-time and high accuracy capabilities. Additionally, these devices can be used for wavefront reconstruction of coherent or incoherent optical beams. One of the main factors that restricts the performance of the SH sensor is the presence of a speckle field in a coherent incoming wavefront [13–19]. The nonlinear response and the restricted dynamic range imaging capabilities of the SH sensor reduce the accuracy (indeed the possibility) of the reconstructed wavefront. This problem typically arises in the cases of ocular wavefront sensing where a strong speckle field is formed by random interference of the coherent laser beam with the highly anisotropic tissues that form the retina [13–17]. Another case is the optical quality measurement of an instrument with rough surfaces [19].

The use of a SH sensor to measure the phase of an incoming wavefront affected by speckle noise is a challenging task. In this case, the different spots have diverse intensity values in the SH CCD plane thus creating bright and dark spots. If the exposure time of the SH sensor is selected to capture clearly the dark spots, then bright ones are lost by overexposure. Likewise, if the integration time is set to sharply capture bright spots, then dark ones are lost in sensor noise. Different solutions for speckle noise reduction have been proposed such as smoothing in software, scanning and descanning mirrors [11,16], or diffusers such as rotating scatterplates, multimode or dispersive fibers [17]. Speckle reduction can also be achieved by decreasing the coherence of the light [17].

Here we propose a purely software-based method to reduce the speckle noise effect. In our case, the philosophy behind the method differs from that in other proposed speckle reduction methods [13–19]. Instead of trying to eliminate the speckle noise in the SH CCD sensor, in our case, its presence is assumed and accepted, and it will be reduced using computer-based methods. The method is based on two steps. In a first step, we used extended dynamic range imaging techniques [20,21] to obtain a high dynamic range (HDR) imaging map of the Hartmann spot diagram that simultaneously captures bright and dark spots. The resultant HDR Hartmann spot diagram is affected by strong background noise and a highly varying modulation map that prevents obtaining the centroids of the Hartmann spot diagram by typical computer vision techniques. For the sake of clarity, Figs. 1(a) and 1(b) show two sinusoidal signals. Figure 1(a) shows a pure sinusoidal signal without background noise and with a constant modulation parameter. In this case, the signal oscillates along the X axis between constant maximum and minimum values. Figure. 1(b) shows a sinusoidal signal as in Fig. 1(a) but affected on the one hand by a linearly increasing background signal and on the other by an increasing modulation parameter. Note in Fig. 1(b) that the peak-to-valley distance and the maximum intensity of each cycle increase along the X axis.

In a second step, a normalization method was used [22] to perform spot diagram background suppression and modulation equalization processes. This method converts a signal affected by background noise and a varying modulation parameter as shown in Fig. 1(b) in a signal without background noise and a constant modulation parameter as shown in Fig. 1(a).

In Section 2 we present the proposed method, Section 3 includes the simulation, the experimental results are presented in Section 4, and conclusions are drawn in Section 5.

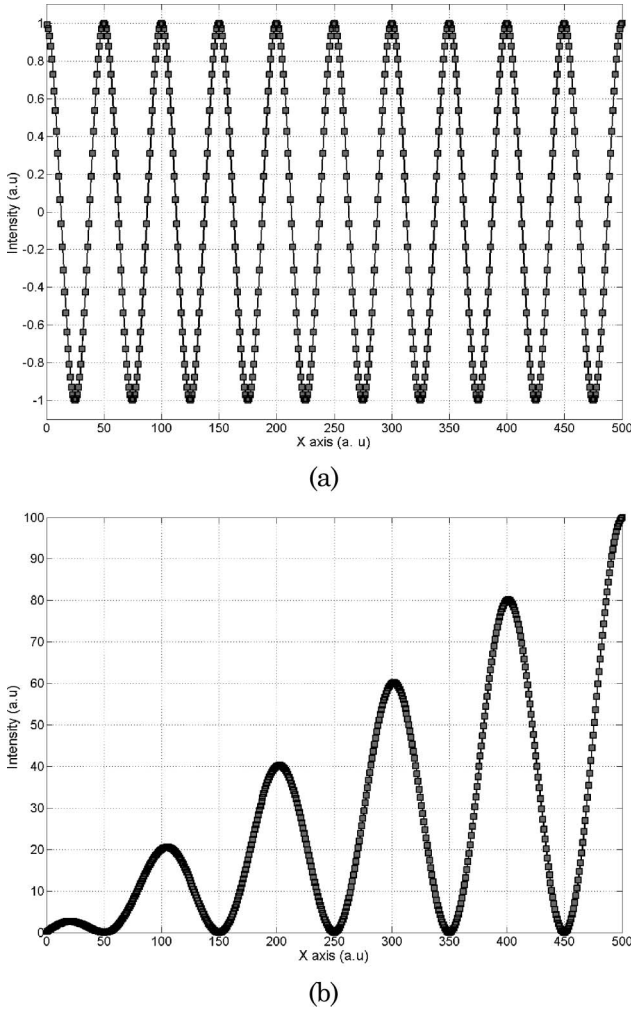

Fig. 1. Sinusoidal signals (a) without and (b) with background noise and (a) constant and (b) varying modulation.

2. Proposed Method

The proposed method used to obtain a suitable Hartmann spot diagram measurement in the presence of strong speckle noise is divided into two steps. In a first step we compute a HDR imaging map of the Hartmann diagram that captures simultaneously very bright and dark spots. In a second step, a normalization process is computed over the HDR Hartmann spot diagram.

A. Constructing the High Dynamic Range Hartmann Spot Diagram

To obtain a HDR measurement we first need to perform a radiometric calibration of the SH CCD sensor. This calibration process consists of obtaining a nonlinear relation between the exposure—product of the incoming irradiance (E) to the SH sensor and its integration time (Δt)—and the returned intensity (I) in gray levels by the SH CCD sensor up to a scale factor. The input of the calibration algorithm is a number of different exposed Hartmann spot diagrams of the same incoming wavefront. The different integration times must be known. The calibration algorithm is based on a regularization method that permits obtaining the SH sensor response function up to a scale factor solving a least-squares problem [20,21]. We assume that the incoming wavefront is static and therefore light changes are ignored. We denote the returned intensity values, in the pixel with lateral coordinates (x,y), by $I_j(x,y)$, where j represents indices over integration times Δt_j. The intensity values are related to the incoming exposure by the nonlinear CCD response curve f:

$$I_j(x,y) = f[E(x,y)\Delta t_j], \tag{1}$$

where f is assumed to be monotonic and therefore invertible. Equation (1) can be rewritten as

$$\ln f^{-1}(I_j(x,y)) = \ln E(x,y) + \ln \Delta t_j. \tag{2}$$

Note that, in Eq. (2), $I_j(x,y)$ and Δt_j are known quantities, and they are needed to recover the function f^{-1} and irradiances $E(x,y)$ that best satisfy Eq. (2). Debevec and Malik [20] presented a least-squares based method to obtain f^{-1} and $E(x,y)$ in Eq. (2) up to a scale factor assuming that the f^{-1} function is smooth.

After the SH sensor response curve is recovered, it can be used to quickly convert pixel values to relative radiance values assuming that the integration time is known [20,21]. In our case, the same Hartmann spot diagrams that were used as input in the calibration algorithm are employed to obtain the HDR Hartmann diagram; therefore, the resultant HDR Hartmann diagram consists in the irradiance map $E(x,y)$ in Eq. (2) computed in the calibration procedure. Typically, to obtain an appropriate HDR Hartmann diagram in the presence of strong speckle noise between 6 and 8, differently exposed spot diagrams are needed. The image with the highest exposure time must capture the dark spots properly; the image with the lowest exposure time must capture the bright spots.

B. Computing the Normalized High Dynamic Range Hartmann Spot Diagram

The intensity distribution of a Hartmann spot diagram can be mathematically modeled as

$$I(x,y) = a(x,y) + b(x,y)\cos[\Phi(x,y)], \tag{3}$$

where $a(x,y)$ is the background illumination, $b(x,y)$ is the centroid amplitude modulation, and $\Phi(x,y)$ is a phase map that models the spot diagram distribution over the SH CCD sensor. In a HDR imaging Hartmann diagram, $a(x,y)$ and $b(x,y)$ usually present a highly varying distribution that makes the automatic and accurate centroid detection process difficult. To overcome this issue, it is possible to carry out a normalization process [22]. This technique allows the contribution of $a(x,y)$ in Eq. (3) to perform a background illumination suppression process. On the other hand, this method carries out a modulation equalization process that transforms the $b(x,y)$ parameter to a constant value. The normalized version of Eq. (3) is

$$I_N(x,y) = b \times \cos[\Phi(x,y)]. \tag{4}$$

This filtering process is useful because it simplifies significantly the spot centroid computation process. In an intensity expression such as in Eq. (4), the different maxima can be obtained from a binarization process that uses a constant binarizing parameter.

The normalization method used in [22] is based on applying a direct and isotropic n-dimensional quadrature operator $Q_n\{\cdot\}$ to Eq. (3). If we assume that the background $a(x,y)$ in Eq. (3) is a spatially smooth function, it is possible to remove it by use of a high-pass filter. We denote $I_{\mathrm{HP}}(x,y)$ as the high-pass filter version of $I(x,y)$. The result of applying the quadrature operator shown in [22] over $I_{\mathrm{HP}}(x,y)$ is given by

$$\begin{aligned} Q_n\{I_{\mathrm{HP}}(x,y)\} &= \mathbf{n}_\Phi(x,y)\mathbf{H}_n\{I_{\mathrm{HP}}(x,y)\} \\ &= -b(x,y)\sin[\Phi(x,y)], \end{aligned} \tag{5}$$

where $\mathbf{n}_\Phi(x,y) = \nabla\Phi(x,y)/|\nabla\Phi(x,y)|$ is a unit vector normal to the corresponding isophasic contours and $\mathbf{H}_n\{I_{\mathrm{HP}}(x,y)\} = \nabla I_{\mathrm{HP}}/|\nabla\Phi|$ is a nonlinear operator that can be interpreted as the n-dimensional generalization of the one-dimensional Hilbert operator. To obtain the normalized version of the intensity distribution shown in Eq. (3), the modulating phase is computed as

$$W\{\Phi\} = \arctan\left(\frac{-Q_n\{I_{\mathrm{HP}}\}}{I_{\mathrm{HP}}}\right), \tag{6}$$

where $W\{\cdot\}$ denotes the phase wrapping operator [23]. Finally, the normalized version of Eq. (3) is

given by $I_N(x,y) = \cos[W\{\Phi\}]$.The exposed normalization method can be applied to intensity distributions as shown in Eq. (3) with complex phase maps assuming the following restrictions; the method needs the background illumination $a(x,y)$ and the centroid amplitude modulation $b(x,y)$ to be spatially smooth and $\Phi(x,y)$ to be derivable.

3. Simulation

To prove the effectiveness of the used normalization method over a Hartmann centroid diagram, we performed a simulation. Figure 2(a) shows a synthetic complex Hartmann centroid diagram with $a(x,y) = 1$ and $b(x,y) = 1$ with the spot centroids superimposed. Figure 2(b) shows the Hartmann centroid diagram that is shown in Fig. 2(a) but with $b(x,y) = 100[\cos(x/100) + 3]$ and the detected spot centroids. Figure 2(c) shows the intensity distribution after applying the normalizing process that is described in Section 2 and the detected spot centroids. Finally, Fig. 2(d) shows the difference between the centroid position obtained from Figs. 2(a) and 2(b) by rectangles and from Figs. 2(a) and 2(c) by circles. The mean values of these differences are 0.056 and 0.23 px (pixel value) and the standard deviations are 0.064 and 0.30 px for the normalized (circles) and nonnormalized (rectangles) images, respectively. As can be seen from the results shown above, the normalization process improves the accuracy of the computed spot centroids.

4. Experimental Results

The SH sensor used for the measurements consists of a Universal Serial Bus (USB) CCD camera with a spatial resolution of 640 px × 480 px and a microlens array from SÜSS MicroTec, Munich, Germany, with 80 × 80 lenses with a geometric focal length of 19.34 mm and a numerical aperture of 0.006.

The proposed technique has been used to measure the optical quality of the MOS, a small aperture imaging optical system included in an optical bench instrument (MIRI Telescope Simulator) used to calibrate the MIRI of the James Webb Space Telescope (JWST). The MOS was designed and integrated in the Space Instrumentation Laboratory (LINES) belonging to Instituto Nacional de Técnica Aeroespacial (INTA). MOS is a point-to-point finite conjugate system with an aperture and focal length of 155 and 3017 mm, respectively, which projects the image of a point source onto the MIRI input plane. This instru-

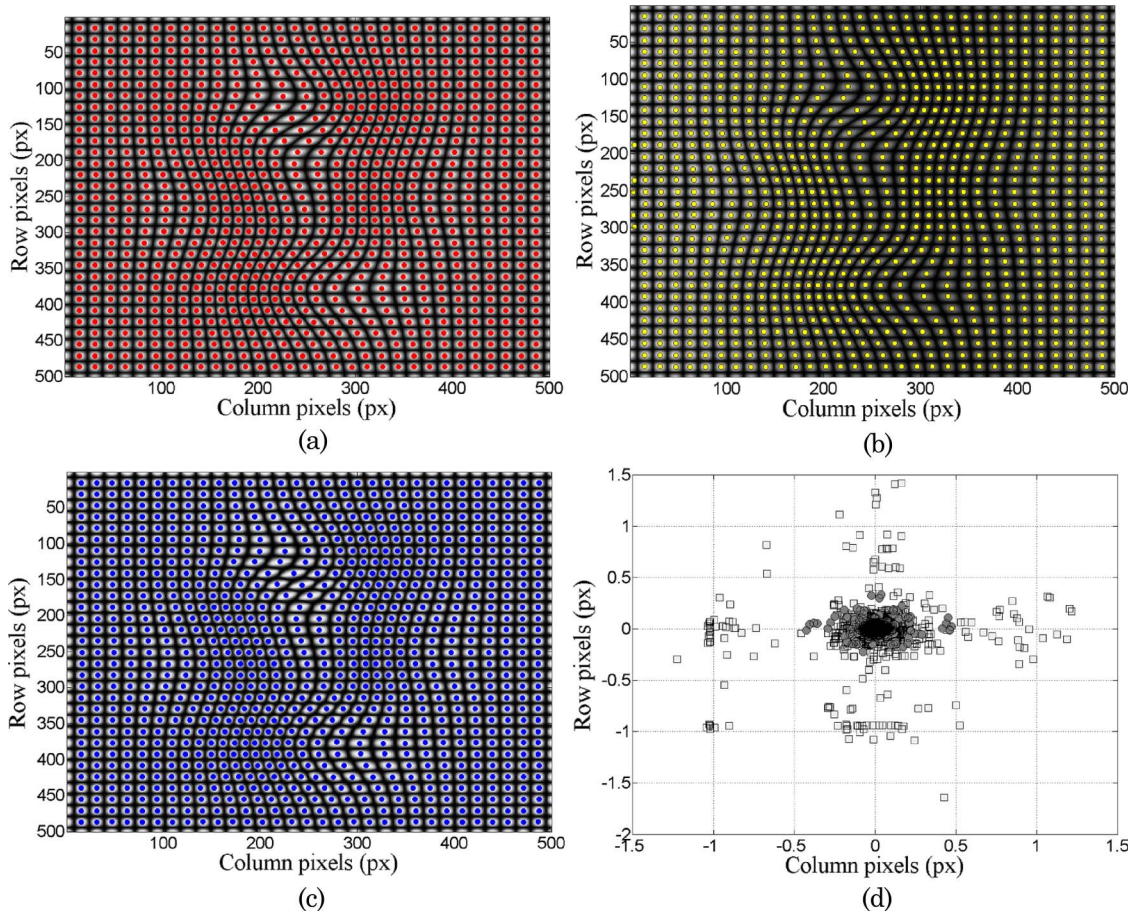

Fig. 2. (Color online) (a) Synthetic complex Hartmann centroid diagram with $a(x,y) = 1$ and $b(x,y) = 1$ with the spot centroids superimposed; (b) Hartmann centroid diagram with $b(x,y) = 100[\cos(x/100) + 3]$ and the detected spot centroids; (c) intensity distribution after applying the normalizing process and the detected spot centroids; (d) difference between the centroid position obtained from (a) and (b) with rectangles and from (a) and (c) with circles.

Fig. 3. Image of the interferometric fringes obtained with the Zygo interferometer.

ment is a catoptric system comprised of two aspheric plates, almost flat, a primary mirror with central obscuration, and a secondary mirror; all the surfaces were made of aluminum, polished with a diamond tip, and gold coated. The MOS was designed to function in the range from 5 to 28 μm and operate together with the MIRI at 35 K during instrument verification and flight model testing campaigns. In spite of the fact that the system must operate in the infrared, it was decided to test the MOS in the visible because of the complexity of testing infrared instrumentation.

MOS optical quality verification was first tried using interferometric techniques. With this purpose in mind, a Zygo GPI-XP phase-shifting interferometer at 632 nm was used in conjunction with a 6 in. (15 cm) beam expander and a custom Fizeau corrector lens. Figure 3 shows an image of the interferometric fringes obtained with the Zygo interferometer. The output of the Zygo was processed using FAST! fringe-tracing software. As can be seen from Fig. 3, we obtained interferograms with very low modulated fringes that were affected by strong speckle noise. The fringe contrast was insufficient to allow automated fringe demodulation processing, and most of the fringe points were placed by hand. These selected points correspond to the small white dots in Fig. 3. With this interferogram it was not possible to obtain reliable wavefront reconstruction. As mentioned, the mirror polishing process makes the optical system sensitive to speckle noise when it is illuminated with a coherent source with a wavelength within the visible spectrum.

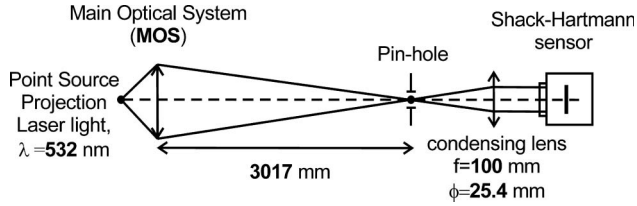

Fig. 4. Scheme of the measuring system.

After the interferometric test, we tried to measure the MOS optical quality with the SH sensor using a laser light. As mentioned above, the MOS surfaces were gold coated. This coating reduced the surface reflectance in the visible spectrum range and made it necessary to use powerful light sources as a laser. Figure 4 shows a scheme of the measuring system. The MOS is illuminated by a green laser source ($\lambda = 532$ nm) and the image is formed at 3017 mm where a small pinhole (less than 100 μm diameter) is located. We placed a 100 mm focal length

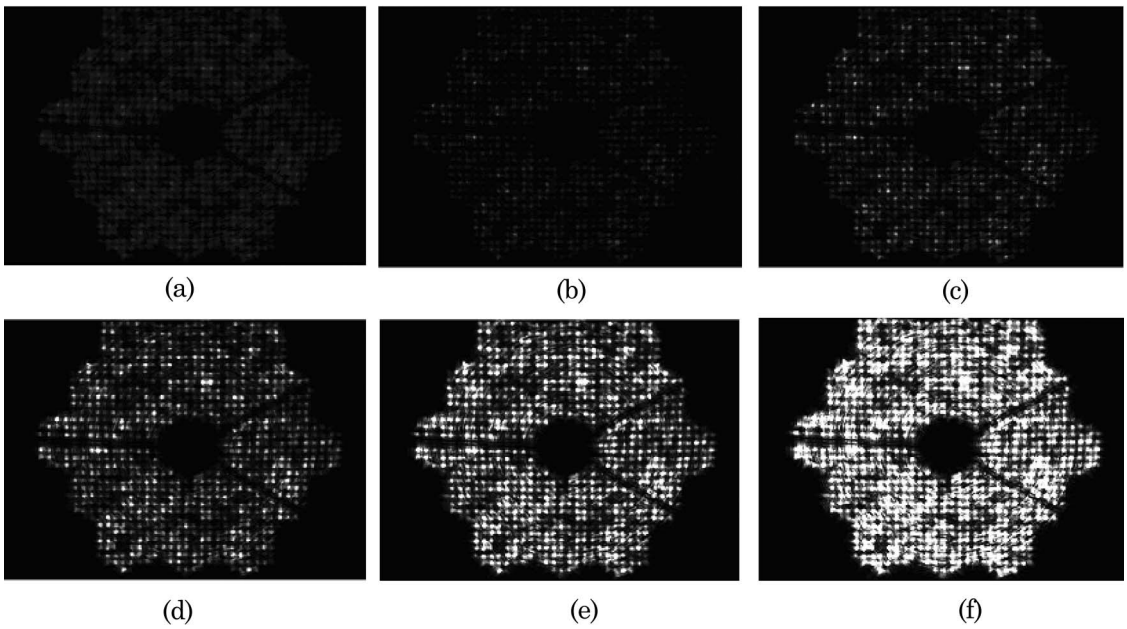

Fig. 5. Hartmann spot diagrams obtained with different exposure times of the SH CCD sensor: (a) 1/8192 s, (b) 1/4096 s, (c) 1/2048 s, (d) 1/1024 s, (e) 1/512 s, and (f) 1/256 s.

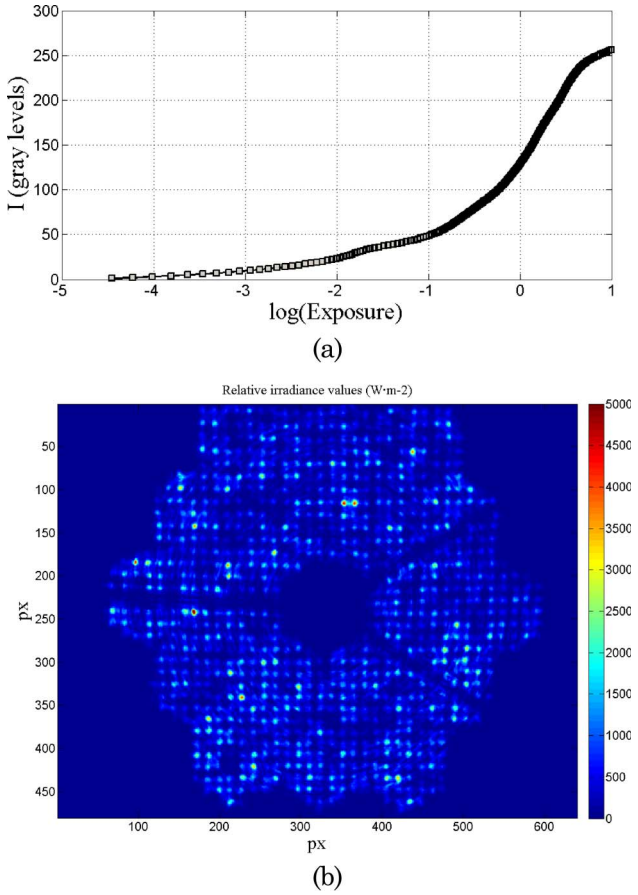

Fig. 6. (Color online) (a) Obtained camera response function (f) and (b) HDR Hartmann spot diagram obtained with the different exposed images shown in Fig. 5.

condensing lens behind the pinhole to obtain a collimated beam on the microlens array of the SH sensor. The relative position between the positive lens and the microlens array was selected to obtain an image of the MOS aperture on the microlens array.

To use the proposed method, we set different exposed images to capture the SH sensor. The values of the integration times were 1/8192, 1/4096, 1/2048, 1/1024, and 1/512, 1/256 s. Images of the differently exposed Hartmann spot diagrams are shown in Fig. 5. As can be seen in Fig. 5, bright spots can be observed properly only in images with low integration times. In the case of high exposure times, bright spots are lost becaise of overexposure. On the other hand, dark spots are recorded properly in images with high integration time. These dark spots are lost in sensor noise in the case of images with low integration times. Figures 6(a) and 6(b) show the resultant camera response function and the HDR Hartmann spot diagram, respectively, obtained with the calibration algorithm. Note that the resultant HDR Hartmann spot diagram is actually a relative irradiance map in units of W/m^2. As can be seen in Fig. 6(b), the dynamic range of the HDR Hartmann diagram varies from 0 to 5000 W/m^2. In Fig. 6(b) it is not possible to observe the bright and dark spots at the same time because of its HDR. Figure 7 shows a tone-mapped transformation of Fig. 6(b) that reduces its dynamic range but reproduces as many image details as possible [24]. In Fig. 7 it is possible to appreciate the dark and bright spots simultaneously. Figure 8 shows the

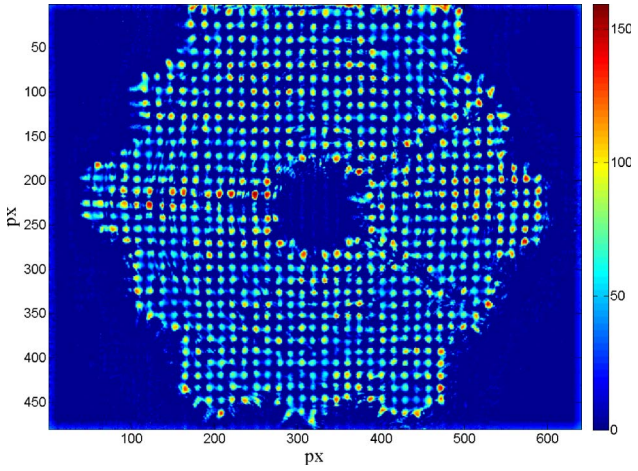

Fig. 7. (Color online) Tone mapped transformation of Fig. 6(b).

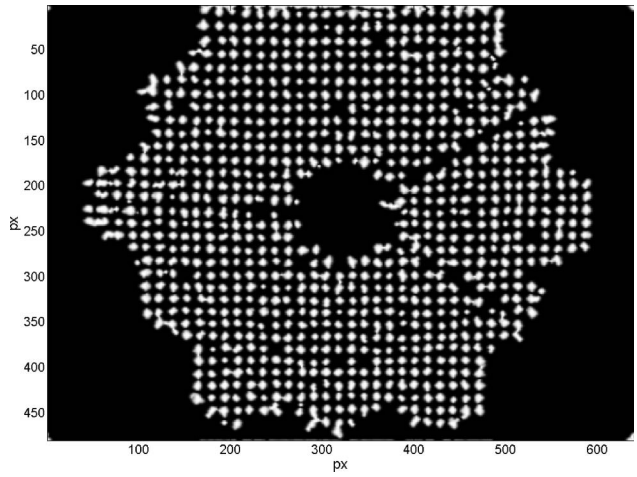

Fig. 8. Normalized version of the HDR Hartmann spot diagram shown in Fig. 6.

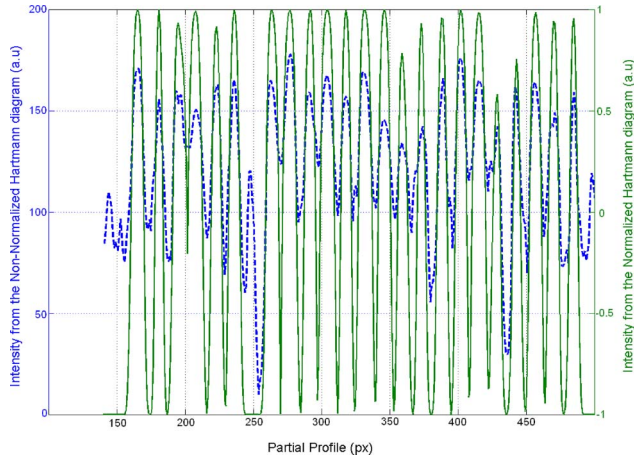

Fig. 9. (Color online) Partial profiles of Figs. 6 and 7 along row 380 and between columns 150 and 490 px.

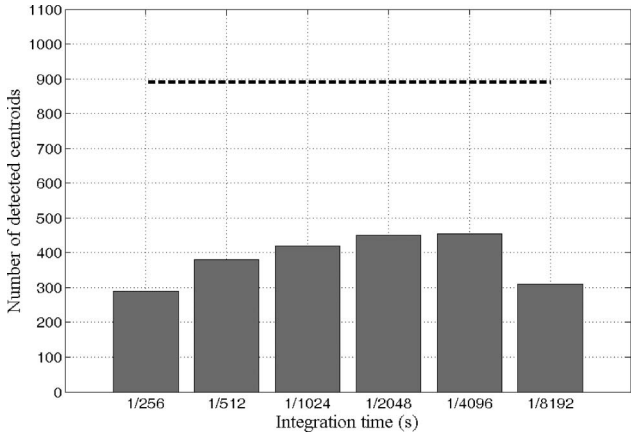

Fig. 10. Plot of the number of detected centroids from the different exposed Hartmann spot diagrams (bars) and obtained from the proposed method (dashed line).

normalized version of Fig. 6(b). Figure 8 shows the high homogeneity of the modulation distribution. Figure 9 shows profiles of Figs. 7 and 8 along row 380 and between columns 150 and 490 px. The dashed and continuous curves in Fig. 9 show the intensity distribution from the nonnormalized and normalized Hartmann diagrams, respectively. As can be seen in Fig. 9, there is a good maximum intensity location correspondence between the dashed and the continuous curves. To show the improvement obtained with the proposed method, Fig. 10 shows a plot of the number of detected centroids from images obtained with a single camera integration time (bar plot in Fig. 10) and using all the integration times by a HDR image (dashed line in Fig. 10). Figures 11 and 12 show the histogram of the Zernike coefficients and the reconstructed wavefront, respectively. Note that, in Figs. 10 and 11, the piston and tilt coefficients have been subtracted as usual. As can be seen in Figs. 11 and 12 the MOS optical system was mainly affected by vertical coma aberration. This vertical coma was caused by a misalignment between the primary and the secondary mirrors that could be corrected. Observe in Fig. 12

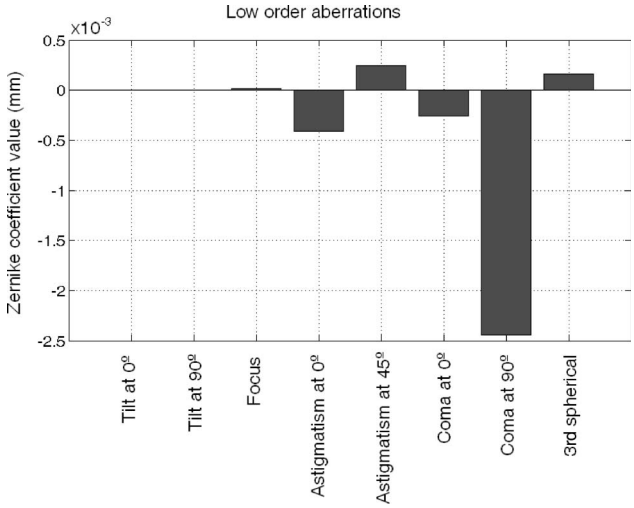

Fig. 11. Histogram of the different Zernike coefficient values.

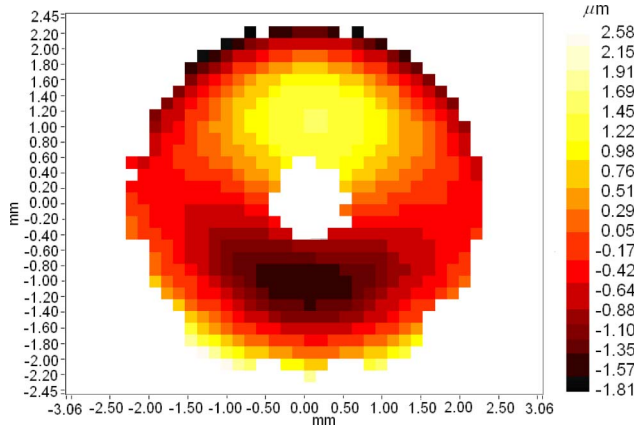

Fig. 12. (Color online) Image of the reconstructed wavefront.

that the region blocked by the central obscuration is not measured because the reconstruction algorithm interpolates only inside small regions. The computed root mean square error is approximately 0.856 μm and the peak-to-valley value of 4.364 μm. Note that this measurement was obtained with a working wavelength of 532 nm.

5. Conclusions

We have proposed a Shack–Hartmann centroid detection method that can be used when strong speckle noise appears in the SH CCD sensor. The method is robust against external disturbances such as air turbulence or temperature fluctuation. This technique can be employed in cases in which traditional interferometric techniques are not appropriate because of the presence of strong external disturbance or speckle noise. The proposed method based on the SH technique does not require any additional hardware component as do other proposed methods, and it is based on a purely software solution. In a first process, a high dynamic range imaging Hartmann spot diagram that simultaneously captures bright and dark spots is computed. In a second step, a normalization process is computed to perform background suppression and a modulation equalization process. The use of the proposed technique permits extension of the dynamic range of the dark spots and therefore improvement in the signal-to-noise ratio and to detect more centroids than when processing a single exposed Hartmann diagram. Therefore, the proposed method improves the lateral resolution and accuracy of the result. The proposed technique has been used to measure the optical quality of the main optical system of the mid-infrared instrument telescope simulator that was used to calibrate the MIRI of the JWST and obtained satisfactory results.

We thank the Ministerio de Ciencia e Innovación of Spain for the financial support of this work given by project “Contribución española al instrumento MIRI del JWST: desarrollo del simulador criogénico del telescopio” with reference ESP2004-01049.

References

1. J. Sheldakova, A. Kudryashov, V. Zavalova, and P. Romanov, "Shack-Hartmann wavefront sensor versus Fizeau interferometer for laser beam measurements," Proc. SPIE **7194** 71940B (2009).
2. B. M. Welsh, B. L. Ellerbroek, M. C. Roggemann, and T. L. Pennington, "Fundamental performance comparison of a Hartmann and a shearing interferometer wave-front sensor," Appl. Opt. **34**, 4186–4195 (1995).
3. R. G. Lane and M. Tallon, "Wave-front reconstruction using a Shack–Hartmann sensor," Appl. Opt. **31**, 6902–6908 (1992).
4. Y. Hongbin, Z. Guangya, C. Fook Siong, L. Feiwen, and W. Shouhua, "A tunable Shack-Hartmann wavefront sensor based on a liquid-filled microlens array," J. Micromech, Microeng. **18** 105017 (2008).
5. Y. Carmon and E. N. Ribak, "Phase retrieval by demodulation of a Hartmann-Shack sensor," Opt. Commun. **215**, 285–288 (2003).
6. J. Ares, T. Mancebo, and S. Bará, "Position and displacement sensing with Shack–Hartmann wave-front sensors," Appl. Opt. **39**, 1511–1520 (2000).
7. R. C. González and R. E. Woods, *Digital Image Processing* (Prentice-Hall, 2007).
8. G. Bradski and A. Kaehler, *Learning OpenCV: Computer Vision with OpenCV Library* (O'Reilly Media, 2008).
9. O. Soloviev and G. Vdovin, "Hartmann-Shack test with random masks for modal wavefront reconstruction," Opt. Express **13**, 9570–9584 (2005).
10. A. Talmi and E. N. Ribak, "Wavefront reconstruction from its gradients," J. Opt. Soc. Am. A **23**, 288–297 (2006).
11. M. Born and E. Wolf, *Principles of Optics* (Pergamon, 1991).
12. V. N. Mahajan, "Zernike polynomials and aberrations balancing," Proc. SPIE **5173**, 1–17 (2003).
13. V. Albanis, E. Ribak, and Y. Carmon, "Reduction of speckles in retinal reflection," Appl. Phys. Lett. **91**, 054104 (2007).
14. A. V. Larichev, P. V. Ivanov, I. G. Iroshnikov, and V. I. Shmalgauzen, "Measurement of eye aberrations is a speckle field," Quantum Electron. **31**, 1108–1112 (2001).
15. J. Liang, B. Grimm, S. Goels, and J. Bille, "Objective measurement of wave aberrations of the human eye with the use of a Hartmann-Shack wave-front sensor," J. Opt. Soc. Am. A **11**, 1949–1957 (1994).
16. H. Hofer, P. Artal, B. Singer, J. L. Aragon, and D. R. Williams, "Dynamics of eye's wave aberration," J. Opt. Soc. Am. A **18**, 497–506 (2001).
17. J. Rha, R. S. Jonnal, K. E. Thorn, J. Qu, Y. Zhang, and D. T. Miller, "Adaptive optics flood-illumination camera for high speed retinal imaging," Opt. Express **14**, 4552–4569 (2006).
18. J. W. Strohbehn, *Laser Beam Propagation in the Atmosphere* (Springer-Verlag, 1978).
19. C. Kiikka, D. R. Neal, J. Kincade, R. Bernier, T. Hull, D. Chaney, S. Farrer, J. Dixson, A. Causey, and S. Strohl, "The JWST infrared scanning Shack Hartmann system: a new in-process way to measure large mirrors during optical fabrication at Tinsley," Proc SPIE **6265** 62653D (2006).
20. P. E. Debevec and J. Malik, "Recovering high dynamic range radiance maps from photographs," in *SIGGRAPH* (ACM Press, 1997), pp. 369–378.
21. J. Vargas, T. Koninckx, J. A. Quiroga, and L. V. Gool, "Three-dimensional measurement of microchips using structured light techniques," Opt. Eng. **47**, 053602 (2008).
22. J. A. Quiroga and M. Servín, "Isotropic n-dimensional fringe pattern normalization," Opt. Commun. **224**, 221–227 (2003).
23. D. Ghiglia and M. D. Pritt, *Two-Dimensional Phase Unwrapping* (Wiley, 1998).
24. E. Reinhard, G. Ward, and S. Pattanaik, *High Dynamic Range Imaging: Acquisition, Display, and Image-Based Lighting*, The Morgan Kaufmann Series in Computer Graphics (Morgan Kaufmann, 2005).